DRAFT
CMS CRAFT Performance Note

The content of this note is intended for CMS internal use and distribution only

2009/08/27
Archive Id: 0.1
Archive Date: 2009/08/24 20:47:31

Performance of the CMS Cathode Strip Chambers with Cosmic Rays

The CSC DPG
CERN

Abstract

The Cathode Strip Chambers (CSC's) constitute the primary muon tracking device in the CMS endcaps. Their performance has been evaluated using data taken during a long cosmic ray run in Fall 2008. Distributions of basic global quantities are well reproduced by the simulation. The anode electronics has been shown to be stable with a very low incidence of inoperative channels. Efficiencies have been measured and are very high, and the spatial resolution of the chambers has been studied and measured, with good results. Finally, a brief exploratory study of the potential timing capabilities of the CSC's has been completed.

1 Introduction

The Cathode Strip Chambers (CSC's) comprise an essential component of the CMS muon detector, providing precise tracking and triggering of muons in the endcaps. Their performance is critical to many planned physics analyses based on muons. An early assessment of their performance is possible using data recorded during the Fall of 2008 as part of the *Cosmic Run At Four Tesla* (CRAFT) campaign. This paper summarizes the early results obtained from the analysis of those data.

The CRAFT campaign involved all installed subdetector systems, most of which were nearly fully operational, as described in other reports included in this volume. Close to 300 M cosmic ray muon triggers were recorded while the magnet was a full field (3.8 T). Of these, roughly a fifth originated from the CSC's.

The CSC subdetector is composed of rings of trapezoidal chambers mounted on eight disks - four in each endcap. The rings of chambers are designated by $ME \pm S/R$, where the $\pm$ sign indicates the endcap, S indicates the disk (or "station"), and R is the ring number. A drawing of CMS highlighting the CSC subdetector is shown in Fig. 1. Each chamber contains six gas layers, with an anode wire plane and two cathode planes, one of which is milled to provide coordinate readout. For details, see Ref. [1]. The CSC's measure the ϕ coordinates of muon tracks well, as the bending of the muon trajectories in the magnetic field returned through the iron disks is mainly about the $\hat{s}$ direction, where $\hat{s}$ is a unit vector in cylindrical coordinates pointing away from the beam line. The strips describe constant ϕ values, and hence are trapezoidal in shape, like the chambers themselves. A high precision is achieved on the basis of the shape of the charge distribution on three consecutive strips; this allows an adequate measurement of the muon momentum as needed for triggering purposes. The anode wires provide a relatively approximate measure of the radial coordinate.

The readout of a CSC is triggered by the presence of Anode and Cathode Local Charged Track patterns, referred to as ALCT and CLCT, respectively. They are defined in the trigger logic [2, 3]. A correlated LCT is also defined and used in triggering the readout of the chamber. A parallel processing of the anode and cathode signals through the CSC track finder produces trigger primitives that are sent to the general muon trigger processor. For CRAFT, events were recorded with a very loose CSC trigger based on the logical "OR" of the trigger signals of all individual chambers.

In the sections that follow, we present a selection of distributions characterizing the useful cosmic ray flux through the endcaps, an assessment of the CSC anode electronics, results on the measurement of efficiency and resolution, and some basic information about the timing capabilities of the CSC's. Most of these results are documented more fully in Ref. [4–7]. We begin with a brief account of the commissioning of the system and of the basics of offline reconstruction.

2 Commissioning the CSC's

The assembly of the CSC's included a comprehensive commissioning regimen to verify chamber performance during production [8]. This set of tests was performed again on each chamber upon arrival at CERN, and multiple times following installation on the endcap disks on the surface during 2005-7. In 2007, the disks were lowered into the CMS cavern at Point 5, and the full set of services and infrastructure became available in January 2008. At this time, a team of physicists and engineers expanded the scope of the commissioning program from checking

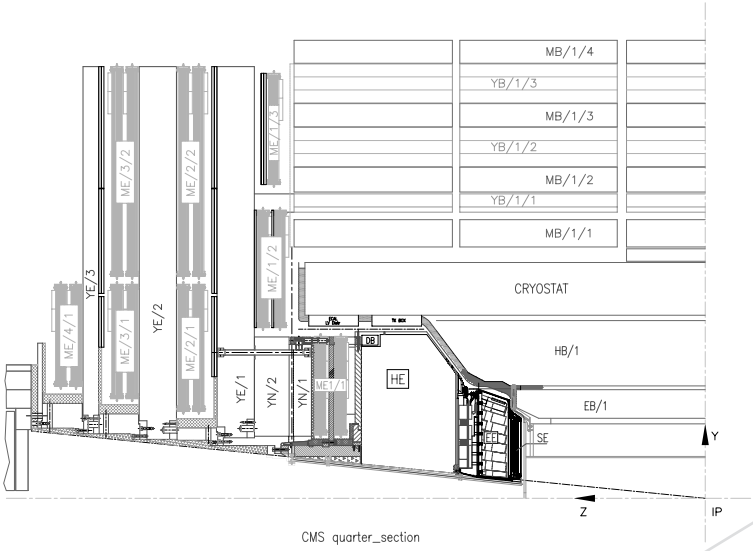

Figure 1: cross-sectional view of the CMS detector, highlighting the CSC's.

one chamber at a time to covering the entire set of 468 chambers as a subdetector system.

The commissioning effort included the following tasks: establishing inter-component communication, loading new versions of firmware to the electronics boards, turning on and configuring all components in a robust way, and measuring the parameters necessary to ensure synchronization of the system. An essential aspect of the commissioning effort was to diagnose what components, including cables, had problems so that they could be fixed before the CMS detector was closed. In addition, the development of a suite of software tools was essential to bring the CSC system online - a system whose size requires procedures and rigor akin to an assembly line. By the time of CRAFT, more than 96% of the readout channels were live. Fig 2 shows that hits could be reconstructed successfully in most of the chambers.

During CRAFT, the CSC's functioned well over a period of several weeks, and they were included in the readout for about 80% of the CRAFT running period. The system was exposed to a different set of issues which had not been encountered during the normal commissioning period.

3 Local Muon Reconstruction

Raw data recorded from the detector are unpacked into integer-based objects called "digis." There are digi collections for the strip signals, the wire signals, and the local chamber trigger tracks (LCT's). The information stored in the digis is processed to produce a collection of objects called "rechits" with measured x and y coordinates at a known z coordinate. These represent the measurement of the intersection point between the track and a CSC layer. The rechits reconstructed in a given chamber are used to form a straight-line segment, which is fit to provide a measure of the muon trajectory in the chamber. Only one rechit is used from any given layer, and a minimum number of three rechits is required. Most segments have six

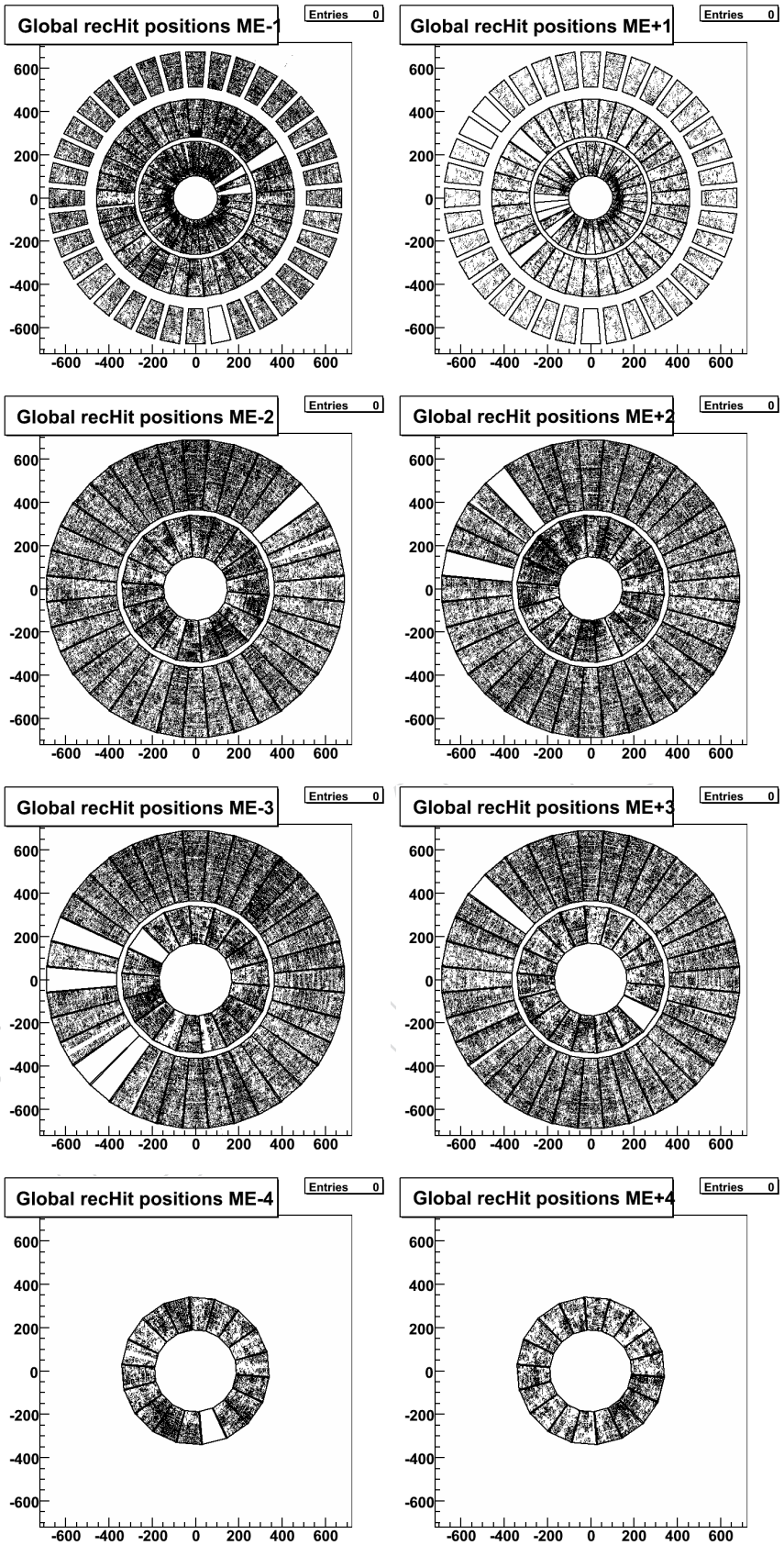

Figure 2: distributions of rechits reconstructed from a portion of the CRAFT data. Nearly all of the chambers were fully operational

rechits. These segments are used to seed the reconstruction of muon tracks based on muon chamber data only – these are called "stand-alone muons" [9]. Due to the very broad flux of cosmic rays through the CMS detector, only a small fraction of the stand-alone muons can be matched to reconstructed tracks in the Silicon tracker, especially those in the endcaps.

The alignment of the muon chambers and of the Si tracker is based on two complementary methods - the first uses lasers and specially placed sensors, while the other uses muon tracks. The first method provided basic information about the position of the endcap disks relative to the barrel, and this information was used in the reconstruction of the CRAFT data. Alignment of the muon endcap detectors with tracks is ongoing. For more details, see Ref. [10] in this volume.

The magnetic field map was verified by examining the deflection selected muon tracks passing through the disks and the Si tracker. It was shown to be accurate to 5% or better [11].

Simulated data sets were produced using the `CMSCGEN` Monte Carlo event generator, which is configured to reproduce the CRAFT data as closely as possible [12]. The simulated data, the reconstructed CRAFT data, and the results presented in this paper are based on official CMS reconstruction code dating from the Spring of 2009.

4 Basic Information from Cosmic Rays

Most cosmic rays above ground have an energy of at most a few GeV [13]. In the underground cavern at Point 5, the energies are shifted to somewhat higher values. Muons must have energies of at least a few GeV in order to pass through three consecutive CSC stations, since the iron disks between them are approximately 34 X_0 thick. Most reconstructed cosmic ray muons have only a few GeV, so multiple scattering in the iron yokes can displace the muon's trajectory by several centimeters with respect to the ideal trajectory.

Most of the muons triggered in the endcaps are not useful because their trajectories are steeply inclined or pass through only an edge of one of the endcaps. Only a minute fraction of the recorded cosmic ray muons follow a useful path through the endcaps, and satisfy the nominal geometric requirements for the efficient triggering and readout of the CSC's, as explained in detail below.

In order to secure a sample of useful events, a skim of the primary data set was performed. The offline program `CSCSkim` identified events in which at least three chambers had hits, and in which at least two segments had been reconstructed. Events with very many rechits or segments were excluded, since they were likely contain muon-induced showers which would frustrate these performance studies. These relatively loose criteria reduced the data sample with CSC triggers by a factor of twenty, and enabled direct comparisons of the simulated data to the real CRAFT data.

Distributions of simple global quantities such as the total number of rechits per event and the number of segments per event are shown in Fig. 3. The requirement of three chambers with hits suppresses entries at the low end of these distributions. One sees a small number of events with two segments even though at least three chambers have hits, which indicates that the chambers do not have many extra hits and that the segment reconstruction is efficient.

Further information about the reconstructed segments is shown in Fig. 4. The first plot shows the number of hits on a segment, which must be at least three and cannot be more than six. Most segments have one rechit in every layer, and this is well reproduced by the simulation.

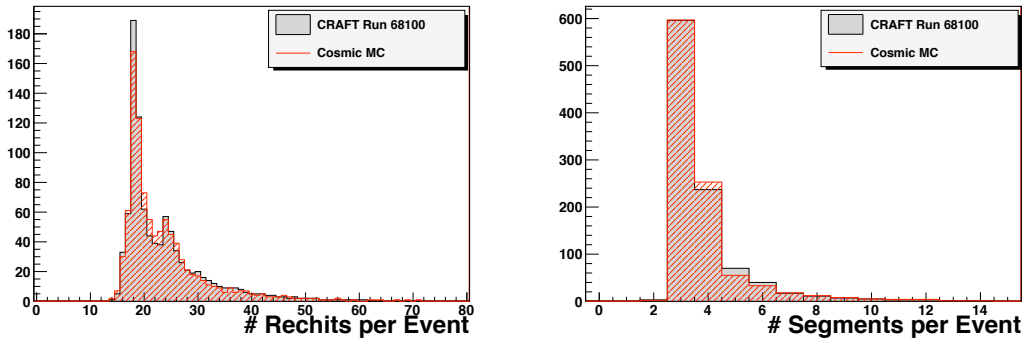

Figure 3: comparison of the simulated events to the real CRAFT events for simple global quantities. *LEFT:* total number of rechits per event. *RIGHT:* total number of segments per event.

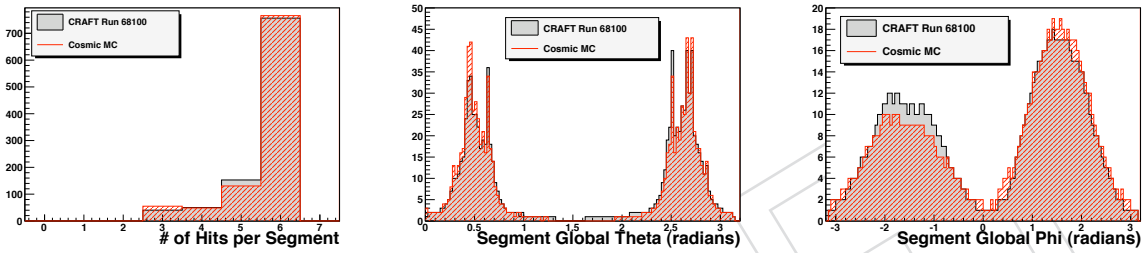

Figure 4: comparison of the simulated events to the real CRAFT events for reconstructed segment quantities. *LEFT:* number of hits per segment. *MIDDLE:* global polar angle. The two endcaps are clearly visible (ME+ at $\theta \sim 0.5$ and ME- at $\theta \sim 2.7$). *RIGHT:* global azimuthal angle. The bump at $\phi \sim 1.8$ corresponds to the upward vertical direction, and $\phi \sim -1.8$, to the downward.

The second and third plots show the inclinations of the segments, namely, the polar angle ("global theta") and the azimuthal angle ("global phi"). The vertical nature of the cosmic ray flux is evident in these distributions, which are very well reproduced by the simulation.

Finally, basic distributions for stand-alone muons in the endcaps are presented in Fig. 5. The first plot shows the distribution of the number of CSC rechits on the track. The distribution of simulated events differs from the CRAFT distribution in part because the alignment of the muon endcaps has not been completed. The second plot shows the polar angle computed at the point on the stand-alone muon track closest to the center of the detector. The agreement is very good.

5 Anode Signals

The anode-wire front-end electronics system was designed with an emphasis on timing precision. The system produces a timing measurement of each anode-wire hit, as well as a coarse measurement of its radial position. The large spread of possible electron drift times in a chamber gas gap, with a maximum of ≈ 50 ns, is compensated for by first requiring a "time stamp" coincidence of anode-wire hits in two layers of a chamber. This "pre-trigger" is then confirmed by demanding a coincidence of four or more hits from different layers in that chamber which form one of a predefined set of track patterns. The 25-ns LHC bunch crossing in which the

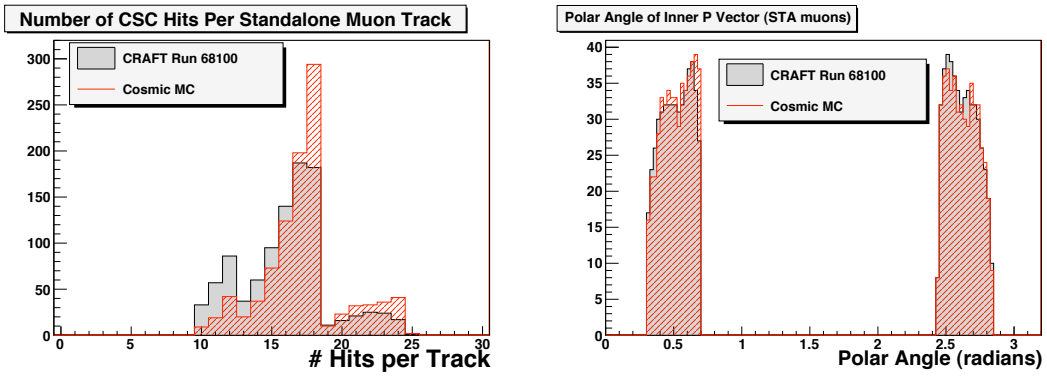

Figure 5: comparison of the simulated events to the real CRAFT events for stand-alone muon tracks. *LEFT:* number of hits per track. *RIGHT:* global polar angle.

track occurred is then found by using the time of the second earliest anode hit from the "pre-trigger" [1, 14]. This procedure is less vulnerable to random-hit backgrounds than using the timing of the first hit, and provides a high-efficiency bunch-crossing identification [14]. The corresponding trigger algorithms are implemented on the ALCT board [15], located on each CSC, which receives the signals from each of the 16-channel anode-wire front-end boards (AFEB). Each ALCT board accepts signals from 12 to 42 AFEB's, depending on the size of the CSC. At the input of the ALCT, the AFEB signals can be delayed by a set of 16-channel programmable delay chips, having 15 delay steps of 2.2 ns each. The ALCT identifies the radial location, bunch-crossing time, and quality of the two best track segments for each CSC, and passes these parameters to the Level-1 trigger system. It also produces a list of all the anode-wire hits in that chamber and in which of 16 consecutive time bins the anode signal arrived, where each time bin is 25 ns long, and the time window begins four time bins before the ALCT trigger is set. This information is then sent to the data-acquisition system.

5.1 Analysis

All events with at least one anode-wire hit are selected for analysis. A key quantity is the number of time bins for which a given anode hit is *on*, denoted here by $N_{\rm on}$. For each CSC, three types of 2-dimensional histograms are produced:

1. the distribution of $N_{\rm on}$ versus the AFEB number in that chamber, to look for noisy AFEB's. Usually, a large number of anode hits $N_{\rm on} > 2$ is evidence for electronic oscillations or pickup noise in that channel.

2. the distribution of the first time-bin number which is *on* versus the AFEB number in that chamber, with a cut requiring $N_{\rm on} \leq 2$ to reduce the bias caused by any electronic oscillations or pickup noise. We use the mean of these distributions (per AFEB and per CSC) to look for timing offsets and to measure the run-to-run timing stability.

3. the number of hits found in each AFEB channel versus the AFEB number in that chamber, to identify dead or intermittent AFEB channels. Patterns of channels and AFEB's with lower occupancy are due to the edges of the high-voltage segments in each layer, where the gas gain and thus the anode-hit efficiency are lower.

The histograms are produced run by run, and also combined together into one summary histogram.

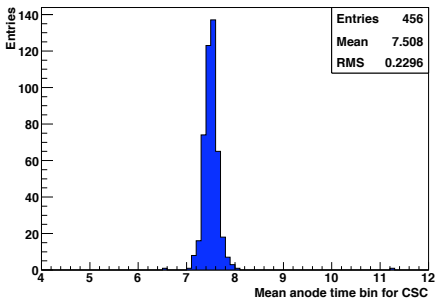

Figure 6: distribution of the mean anode-wire time values for all CSC's in fractions of a time bin, where a time bin corresponds to 25 ns.

5.2 Results

Large runs were analyzed based on raw data, with no filtering of events aside from the requirement of anode wire hits in the CSC's. Approximately 50M events were analyzed from 80 runs spanning the entire CRAFT data-talking period. The sections below discuss results obtained for the anode-board timing, noise, and dead channels.

5.2.1 Anode-board timing

The overall time resolution of the anode front-end electronics is quite good – an r.m.s. of about 0.6 ns for an input signal corresponding to a charge $Q_{in} \geq 100$ fC, and a maximum slewing time of ≈ 3 ns for input charges in the range $Q_{in} = 60 - 600$ fC. The spread of the propagation times within individual AFEB's has an r.m.s. of 1.3 ns [16]. All of these times are small compared to the variation of drift times in a single chamber gap, which has an r.m.s. of about 12 ns.

Fig. 6 shows the mean of the anode-hit time distribution for all CSC's in the entire CRAFT data set in fractions of a time bin, BX, which is 25 ns long. The distribution is almost entirely within one time bin and has an r.m.s. of about 0.2 BX.

5.2.2 Noisy AFEB's

With a typical detector input capacitance of 180 pF, the average intrinsic noise of the AFEB's was measured in Ref. [16] and found to be ≈ 1.4 fC, with a maximum < 1.6 fC. The nominal setting for the AFEB charge discriminator thresholds for CRAFT was 20 fC. At such a threshold, the high-voltage plateau for the anode-hit efficiency of the non-ME1/1-type chambers is ≈ 3.4 - 3.5 kV. The nominal high-voltage setting for these chambers during CRAFT running was 3.6 kV. For the ME1/1 chambers [17], with a smaller gas gap and thinner wires than the other chambers, the high-voltage setting was 3.0 kV.

To monitor the noise in each AFEB, the $N_{\rm on}$ for anode hit was used (see Fig. 7). The fraction of hits with $N_{\rm on} > 2$ was found to be the most discriminating parameter. Such cases are often due to AFEB preamplifier oscillations (threshold too low) or to an increased level of pickup noise.

For the overall presentation of the AFEB noise level in all CSC's in the CRAFT data, the fraction of anode hits with $N_{\rm on} > 2$ is calculated for each AFEB in a CSC, and the maximum fraction for each CSC is then plotted as in Fig. 8. The small gaps in this 2-dimensional histogram are due to the 12 CSC's which were excluded from the data taking for various maintenance reasons. The histogram shows that most of the chambers have a maximum noise rate $< 1\%$, integrated over all runs .

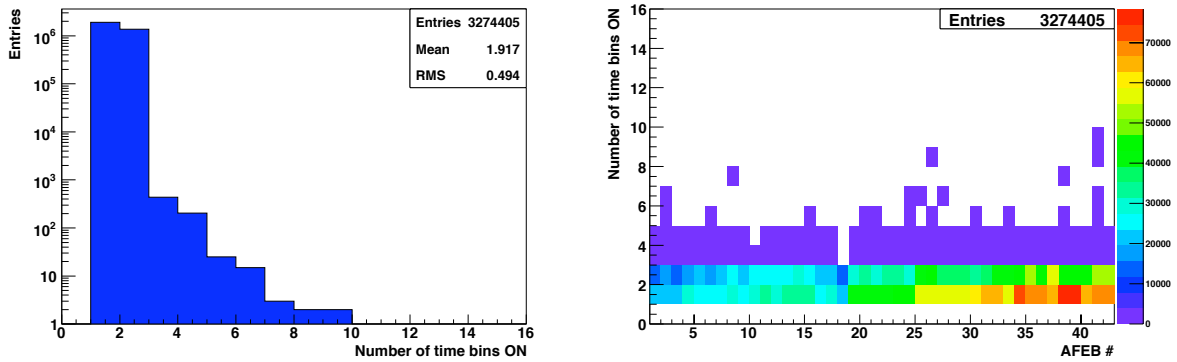

Figure 7: *Left:* A semi-log plot of the number of time bins on for all AFEB's in CSC ME-2/1/9. *Right:* The number of time bins on vs. AFEB number for CSC ME-2/1/9.

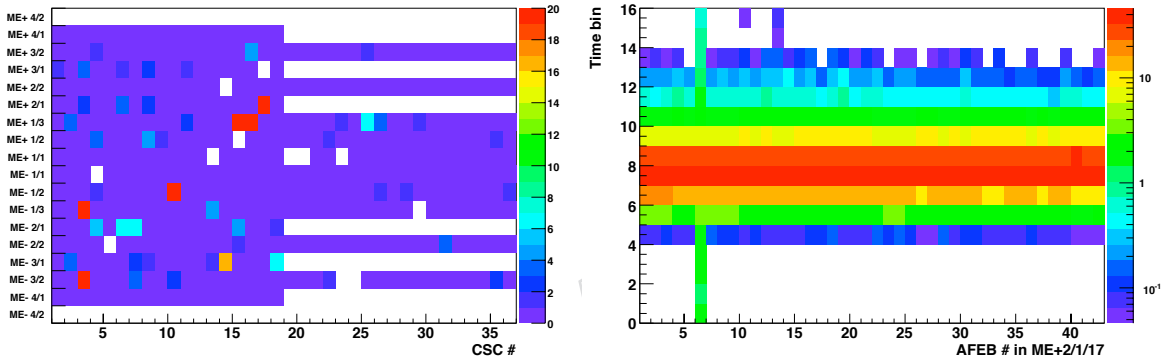

Figure 8: *Left:* The maximum fraction (%) of anode hits with $N_{\text{on}} > 2$ per CSC vs. CSC number in each endcap station. *Right:* The time bin number on vs. AFEB number (normalized per AFEB, %) for CSC ME+2/1/17 in run 68279, showing the effect of pickup noise in AFEB #6.

For noisy AFEB's the occupancy in time bins outside of the peak (see, for example, Fig. 8 for ME+2/1/17, AFEB #6) remains (though reduced), despite the fact that the plot required $N_{\text{on}} \leq 2$. Therefore, another possible criterion for identifying pickup noise could be the fraction of hits with the first two time bins on. However, this occupancy will rise in high-luminosity pp collisions at the LHC due to random hits caused by low-energy neutrons from hadronic interactions, so this diagnostic may be most reliable with cosmic ray events.

A conservative estimate for the total number of noisy AFEB's in the CRAFT run, ignoring the contributions from chambers with known, repairable problems, is ≈ 8 boards out of a total of 11 166 (0.072%).

5.3 Dead and Intermittent Anode Channels

To identify which AFEB channels were dead during the entire CRAFT run, we used plots of the summary histograms showing the total number of hits in each AFEB channel versus AFEB number. Figure 9 gives an example of such a histogram for chamber ME-4/1/2, from which we see that channel #2 in AFEB #11 and channel #11 in AFEB #12 were unresponsive for the entire run. The total number of such dead anode channels was 9 out of a total of 178 656 (0.005%).

Figure 9 gives examples of anode channels with an intermittent signal response. Being an

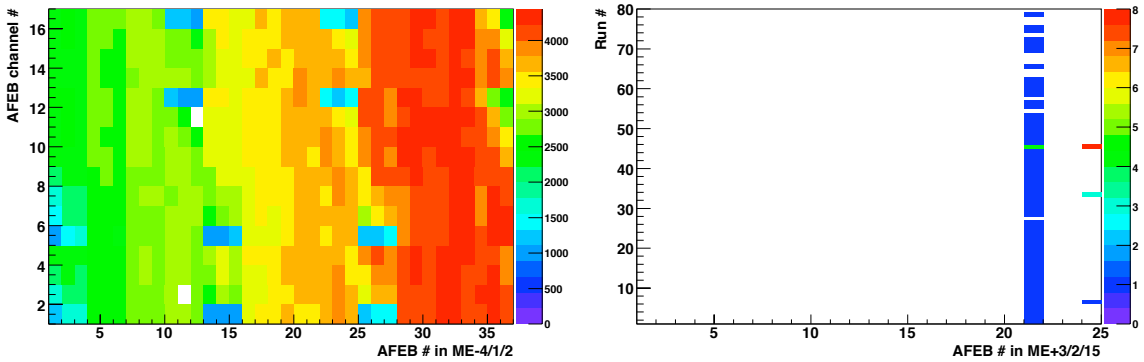

Figure 9: *Left:* The number of hits in each AFEB channel vs. AFEB number for CSC ME-4/1/2. *Right:* The number of channels with no hits vs. run number for each AFEB in ME+3/2/15.

intermittent problem, it is difficult to diagnose the cause of such effects. The total number of such channels was 61 (in 17 AFEB's) out of a total of 178 656 (0.034%).

5.4 Summary

An analysis of data from the CSC anode-wire front-end electronics collected during the CRAFT run shows an excellent performance of the overall system. The anode timing was very stable during the entire data taking. Very low fractions of noisy AFEB boards (0.072%), dead channels (0.005%), and channels with intermittent signals (0.034%) were found.

6 Efficiency

The goal of this study is to measure the absolute efficiency of each step in the reconstruction of muons in the CSC's, from the generation of ALCT's and CLCT's through to segment reconstruction. By design, for good muons coming from the interaction point, all steps should be highly efficient. The method described here uses two chambers to "tag" a muon that passes through a designated "probe" chamber. When computing the efficiency of each step, the same tagged sample (i.e., the "denominator" in the efficiency calculation) is used for all steps.

For efficiency measurements, we need a well-defined muon track which is independent of the measurements in the chamber under investigation. We use muon tracks reconstructed in several CSC's without any information from the Si tracker – these are the "stand-alone" muons. The number of useful stand-alone muons is adequate for the present purposes, thanks to the redundancy of the muon endcap system. To minimize the impact of possible difficulties coming from multiple scattering, energy loss, and tracking in a strong magnetic field, a chamber is probed only if it lies between the endpoints of the track. Consequently, at least two independent measurements of the muon track are needed, and only interpolation and not extrapolation to the probe chamber is used. Some rings, namely ME$\pm$1/1, ME$\pm$4/1 and ME$-$3/2 cannot be covered by this study, although hits in the Resistive Plate Chambers (RPC's) allow coverage of ME$+$3/2.

A typical event selected for these efficiency measurements contains three or four CSC's contributing to a good stand-alone muon track. Since the trigger efficiency is generally high (see below), and a trigger from any one of these chambers sufficed to produce a trigger for read out of CMS, we assume that any trigger bias in the results is negligible.

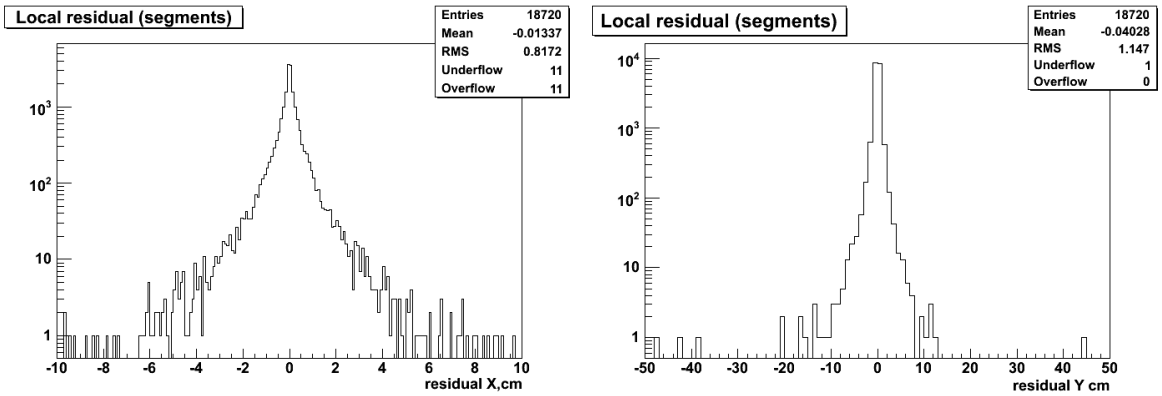

Figure 10: differences between the predicted positions of a segment and the position of the reconstructed segment in the probe chamber. ΔX is on the left, and ΔY is on the right, where X and Y are local coordinates. X is measured primarily by the strips, and Y, by the wires

We place cuts on the predicted position of the muon in the probe chamber to avoid losses due to insensitive regions at the periphery of the chamber and at the boundaries of the high voltage segments. Fig. 10 shows distributions of the difference between the measured position of a segment in the probe chamber and the predicted position, obtained by propagating the muon track from another station to the probe chamber, taking the magnetic field, multiple scattering and energy loss into account. In this figure, the local coordinate X runs parallel to the wires, and is measured primarily by the strips, while Y runs perpendicular to the wires, and is measured by the wire signals. According to these distributions, nearly all of the tracks fall within 10 cm of the predicted position.

A set of stringent criteria is used to selected "good" tracks for the denominator of all efficiency calculations [5]. Only one stand-alone muon track is allowed in an endcap. This track has to have at least a minimum number of hits, and to be reconstructed well, as indicated by the χ^2 and the relative error on the momentum. The momentum itself should be in a reasonable range, $25 < p < 100\,\mathrm{GeV}/c$. A good track satisfying these requirements is propagated to a designated ring of CSC chambers to ascertain which chamber is the probe chamber. If the interpolated point lies within 10 cm of the edges of the chamber or dead regions defined by high voltage segment boundaries, then the chamber is skipped. The tracks which pass all of these criteria are the "probe" tracks.

6.1 Results from CRAFT

The following sections report the details of the measurements and the values of the efficiency for each step in the CSC local reconstruction.

6.1.1 LCT Efficiencies

The ALCT and CLCT efficiencies are measured independently. For a given chamber, the ALCT and CLCT digis are unpacked to test for the presence of a valid ALCT or CLCT. If they are present anywhere in the chamber, then the trial is a "success" and the chamber is "efficient" for that event.

The ALCT wire patterns and the CLCT strip patterns were designed to be efficient only for muons originating from the interaction point [3]. The wire group width varies between 1.5 and 5 cm for different chambers. The distance between layers is 2.54 cm, except for the ME1/1 chambers, for which it is 2.2 cm. The range of track inclination (dy/dz in local coordinates)

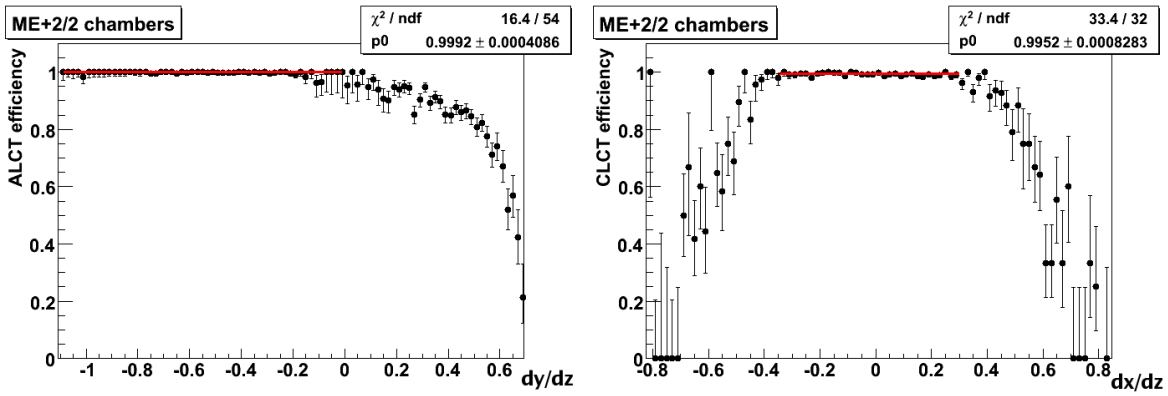

Figure 11: LEFT: ALCT efficiency as a function of the track inclination, dy/dz in local coordinates. RIGHT: CLCT efficiency as a function of the track inclination, dx/dz in local coordinates

which should give efficient ALCT response is $-0.69 < dy/dz < 0$ for smaller chambers, and $-1.97 < dy/dz < 0$ for larger chambers. Similarly, for the CLCT response the range is $|dx/dz| < 0.24$ for smaller, and 0.63 for larger chambers. For collision data, the muons will naturally have inclination angles within these ranges. Muons from cosmic rays, however, arrive at a wide variety of angles. To suppress the muons which are not likely to fire the ALCT and/or CLCT triggers, we apply cuts on the slopes of the muon tracks interpolated through the chamber:

$$-0.8 < \frac{dy}{dz} < -0.1 \qquad \text{and} \qquad \left|\frac{dx}{dz}\right| < 0.2. \tag{1}$$

One could adjust these ranges for the various rings of chambers, but the impact on the efficiency measurements is negligible. All the efficiencies measured with CRAFT data include these requirements in the event selection.

The variation of the ALCT efficiency as a function of dy/dz is shown in Fig. 11 (left). For this figure, the cut on dy/dz was not applied, although the cut on dx/dz was applied. Similarly, the variation of the CLCT efficiency as a function of dx/dz is shown in Fig. 11 (right), with the cut on dx/dz relaxed, and the cut on dy/dz applied. The results shown in these plots are based on data from chambers 5–13 in ring ME+2/2 which were known to be operating well. In both figures, clear plateaus can be seen which were fit with level functions to ascertain the efficiency. Very high values in excess of 0.999 are observed.

6.1.2 Strip and Wire Group Efficiencies

In principle, the presence of an ALCT and CLCT should trigger the read out of the chamber, and hence, signals on the wires and strips should be present in the raw data, or equivalently, in the strip and wire digis. The efficiency for strip and wire digis are measured independently. The probe is given by a good track passing through the given chamber.

The efficiencies of strips, wire groups and rechits are defined naturally per layer. If the layer measurements are independent, then the average efficiency per chamber would be

$$\bar{\epsilon} = \frac{\sum_i \epsilon_i}{L} = \frac{\sum_i n_i}{N \times L} \tag{2}$$

with an estimated uncertainty of

$$\Delta\bar{\epsilon} = \sqrt{\frac{\bar{\epsilon} \times (1 - \bar{\epsilon})}{L \times N}}, \tag{3}$$

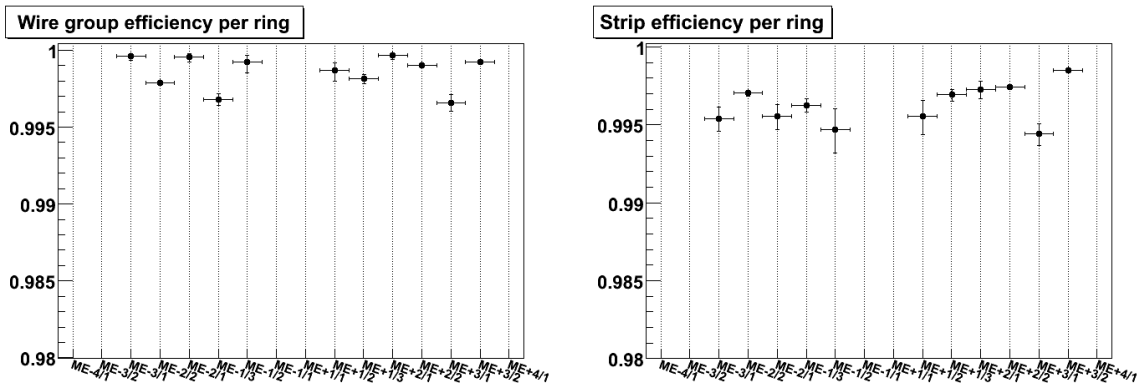

Figure 12: summary of wire group (left) and strip (right) digi efficiencies, over all functioning chambers in a ring. Some rings are inaccessible in this study with CRAFT data.

where $L = 6$ is the number of layers, ϵ_i is the efficiency in layer i ($i = 1, .., 6$), n_i is the number of efficient cases ("successes") for layer i, and N is the number of probe tracks. In principle, there might be events with a simultaneous loss of information from all six layers, in which case Eq. 3 is incorrect. There is no evidence for any such correlated losses.

The average wire group and strip digi efficiencies are shown in Fig. 12. Typically, all six layers are highly efficient, greater than 99.4%.

6.1.3 Rechit Efficiency

The efficiency for reconstructing a rechit is measured for each layer in a chamber. The chamber is efficient if the rechits are found in a given layer - there is no requirement on the distance between the rechit and the interpolated point. Also, no quality requirements are placed on the individual rechits as part of the measurement of rechit efficiency.

The rechit efficiency will be a convolution of the strip and wire group digi efficiencies. It might also depend on some of the details of the rechit reconstruction algorithm, especially as regards quality or other criteria applied to the strip and wire signals. The rechit efficiency for all the CSC rings is shown in Fig. 13. The rechit reconstruction efficiency is above 99.5%.

6.1.4 Segment Efficiency

It should be possible to build a segment if at least three good rechits are recorded along the muon trajectory. The chamber is efficient if a segment has been reconstructed. No matching criteria have been applied (cf. Fig. 10).

Ideally, the segment efficiency would be related in a simple and direct way to the rechit efficiency. The segment reconstruction algorithm, however, also places requirements on the rechits used to build segments. It does not find segments in chambers with very many hits, due to prohibitive combinatorial problems – this will register as an inefficiency in the present study. The segment efficiency for all the rings in the CSC system is shown in Fig.13. For all rings, the segment efficiency is consistent with 99% or larger, for cosmic ray muons.

6.1.5 Attachment Efficiency

The attachment efficiency is a characteristic of the segment finder. It is defined as the probability of the segment to use a rechit from a given layer if there are rechits in that layer. As the segment finder could reject some rechits if their quality were poor, or if they were producing a bad fit, a very high value of the attachment efficiency is not the ultimate goal. What is

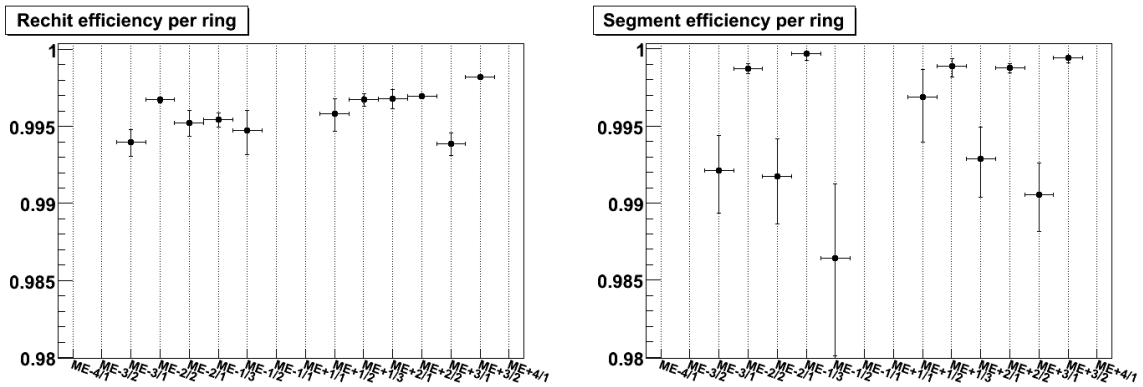

Figure 13: summaries of rechit and segment efficiencies, analogous to Fig. 12

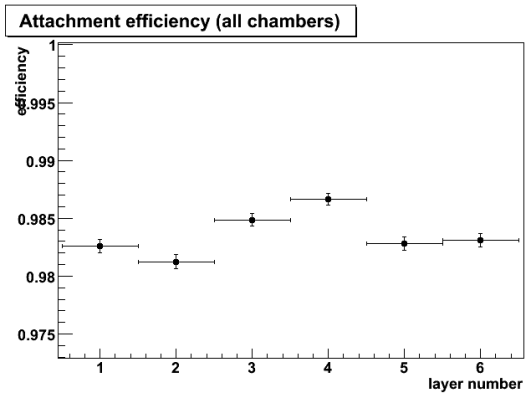

Figure 14: attachment efficiency for each layer

important is that this efficiency should be reasonably flat as a function of the layer number. Any significant variation with layer number would be a hint of a problem – for example, an unacceptable dependence on the track angle. Fig. 14 shows that there is no bias in the CRAFT data.

6.1.6 Summary

In summary, all the basic efficiencies have been shown to be high, for chambers in good operating condition during CRAFT. See Table 1.

quantity	typical efficiency (%)
ALCT	> 99.9
CLCT	> 99.9
wire digis	> 99.5
strip digi	> 99.4
rechit	> 99.2
segment	> 98.5

Table 1: summary of efficiencies for chambers in good operating condition

7 Resolution

The CRAFT data were used to study and measure the spatial resolution of the CSC's as they are meant to be operated for early physics [1]. The purpose of this study is to demonstrate that all working chambers perform as they should, before colliding beams commence. Excellent earlier studies of CSC spatial resolution can be found in Ref. [18, 19].

The following sections define what we mean by "resolution," and how we measured it. We show the expected variations of the resolution as functions of charge, position within a strip, the width of the strip, and angle. Special studies have been carried out for ME$\pm$1/1 chambers, as their design differs somewhat in order to cope with the high magnetic field and difficult demands for resolution [17]. We report measured values of the resolution for all types of chambers, and then conclude.

7.1 Analysis

The reconstruction of muon trajectories and the measurement of the muon momentum depends critically on the spatial resolution of the chambers. The most important coordinate is ϕ, so these studies are concerned with the strip measurements only. An adequate measurement of R at a given z is given by the anode wires.

7.1.1 Methodology

The *resolution* is the typical measurement error. It is determined by the design parameters of the chamber (width of the cathode strip, distance to the anode wire plane, high voltage, anode wire radius and pitch, gas mixture, electronics noise and cross talk) as well as certain characteristics of each muon track (angle, position with respect to the center of the struck strip, and amount of charge collected), and of course the physics of multi-wire proportional chambers (electron diffusion, magnetic field influence) and the reconstruction (reduction of data and knowledge of misalignments). The distribution of hit residuals with respect to the muon trajectory can give a good measure of the resolution. A *residual* is the difference between the measured coordinate and the true or estimated true (i.e., predicted) coordinate.

For the purposes of the study, the coordinate of interest is the coordinate measured by the strips. In global coordinates, this would be $R\phi$ as measured in centimeters, but most of the results presented here are couched in *strip coordinates*. The strip coordinate, s, is the $R\phi$ coordinate relative to the center of the strip, divided by the strip width at the position of the hit. Modulo resolution effects, one has $-0.5 \leq s \leq 0.5$. Most of the plots here will show residuals distributions in strip coordinates. In order to obtain a resolution in physical units, we multiply by the mean width of a strip in the given chamber. A synopsis of relevant chamber parameters is given in Table 2.

The residuals distribution is not Gaussian, in general, so one must settle on a measure of the residuals distribution to be identified with the "resolution" of the given chamber. Usually we fit the distribution with a sum of two Gaussian functions, with zero mean, using the functional form:

$$f(x) \equiv \frac{A_1}{\sqrt{2\pi}\sigma_1} \exp\left(\frac{-x^2}{2\sigma_1^2}\right) + \frac{A_2}{\sqrt{2\pi}\sigma_2} \exp\left(\frac{-x^2}{2\sigma_2^2}\right) \quad (4)$$

[1] The current high voltage settings are intentionally lower than what was used for the test beam studies, in order to avoid aging the chambers unnecessarily during commissioning periods. This has a significant impact on the spatial resolution, as described below

ring	chambers per ring	strips per chamber	strip width (mm)	(mrad)
ME$\pm$1/1a	36	48	4.11 – 5.82	3.88
ME$\pm$1/1b	36	64	4.44 – 7.6	2.96
ME$\pm$1/2	36	80	6.6 – 10.4	2.33
ME$\pm$1/3	36	64	11.1 – 14.9	2.16
ME$\pm$2/1	18	80	6.8 – 15.6	4.65
ME$\pm$2/2	36	80	8.5 – 16.0	2.33
ME$\pm$3/1	18	80	7.8 – 15.6	4.65
ME$\pm$3/2	36	80	8.5 – 16.0	2.33
ME$\pm$4/1	18	80	8.6 – 15.6	4.65

Table 2: selected relevant physical specifications of the cathode strip chambers. For more information, see Ref. [1]

where optimal values for the parameters σ_1, σ_2, A_1 and A_2 are obtained from the fit. We take the resolution to be:

$$\text{resolution :} \qquad \bar{\sigma} = \sqrt{\frac{A_1\sigma_1^2 + A_2\sigma_2^2}{A_1 + A_2}}. \tag{5}$$

If one Gaussian suffices, then we take simply the σ parameter of the single Gaussian. We do not take the r.m.s. as the residual distributions often have long non-Gaussian tails which inflate the r.m.s. - these tails are caused by δ-ray electrons and fall outside a discussion of the core resolution. The residuals distributions of the eight chamber types with fits to Eq. 4 are given in Fig. 15.

As defined, the resolution $\bar{\sigma}$ pertains to a hit in a *single layer*. The resolution of a chamber is more complicated, since it depends on the number of hits in the segment, the angle of the segment, the generally non-normal angle between wire groups and strips, and the fact that the strips are staggered layer-by-layer for all chambers except ME$\pm$1/1. We can take the special case of segments with six hits that are normal to the chamber and pass through the center. If the residuals distribution near the edge of a strip has Gaussian width σ_e, and near the center of a strip, σ_c, then to a good approximation, the resolution for the segment is

$$\text{segment :} \qquad \sigma_{\text{seg}} = \left(\frac{3}{\sigma_e^2} + \frac{3}{\sigma_c^2}\right)^{-1/2}. \tag{6}$$

We will use this expression to characterize the chamber resolution.

Another method for measuring the resolution does not rely on the residuals of a single layer, but rather on the value of χ^2 for the linear fit to all six hits. Let us define the *unweighted* χ^2 as follows:

$$\chi_0^2 \equiv \sum_{i=1}^{6} \left(s_i - (a + bi)\right)^2 \tag{7}$$

where a and b are free parameters, and i plays the role of the z coordinate. Notice we have set all uncertainties to one. As a consequence, $\langle\chi_0^2\rangle = 6\sigma_0^2$, where σ_0 is the effective uncertainty on s_i.

We do not have a good exterior measure of the position of the muon, so we have to use the segment itself. Perhaps the cleanest procedure is to use five out of the six hits on a good segment to predict the position of the sixth. In practice, we fit the hits in layers 1, 2, 4, 5 and 6 to a straight line to predict the "correct" position in layer 3, and then compare to the measured

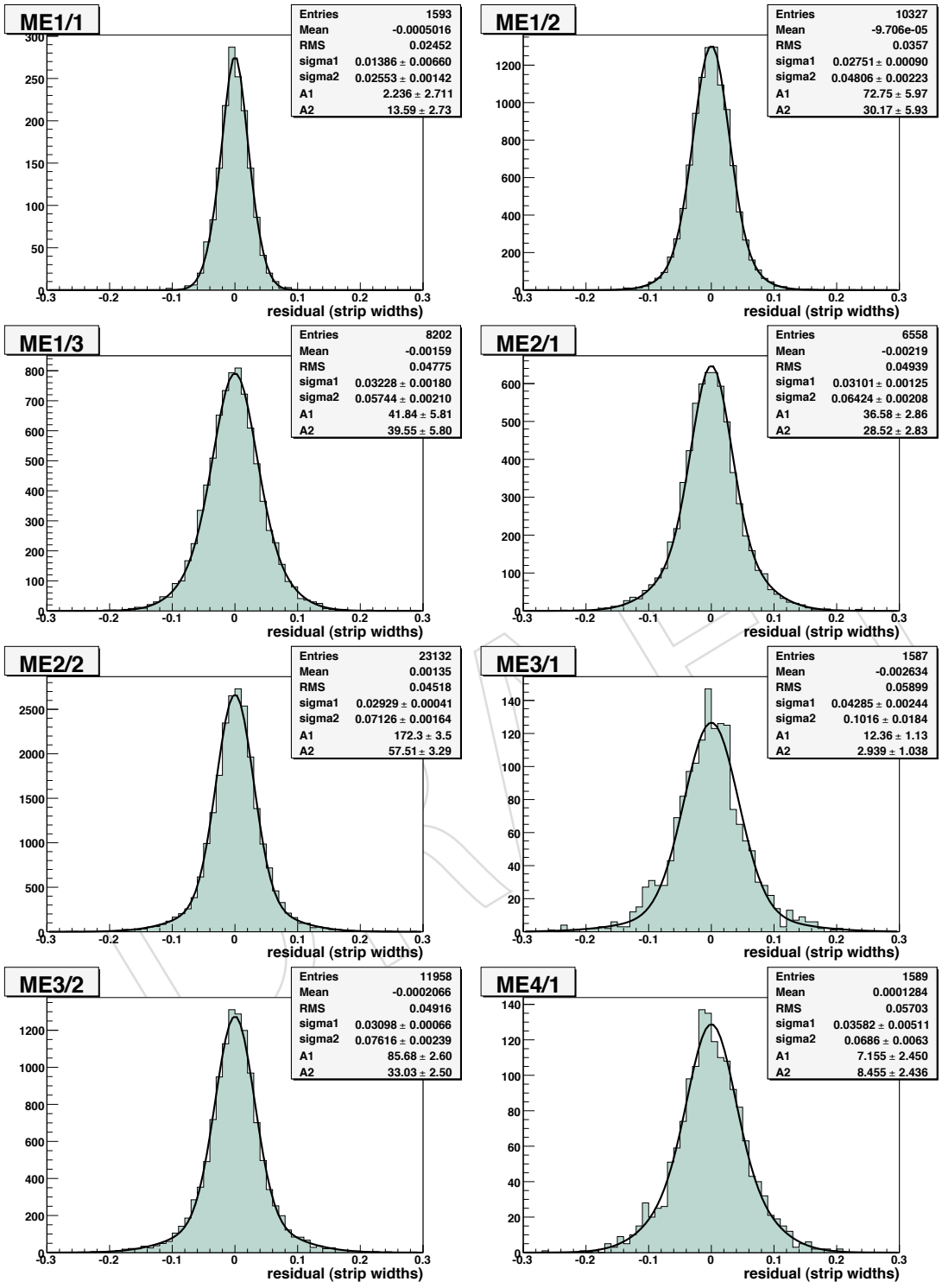

Figure 15: residuals distributions fit to the double-Gaussian function given in Eq. 4.

position in layer 3. Monte Carlo studies show that the width of the residuals distribution is inflated by about 10% due to the measurement error from the five-hit fit; this uncertainty is larger for layers 1, 2, 5 or 6. We do not remove this 10% inflation for the results reported in this note.

7.1.2 Expected Behavior

The resolution is known to vary with several quantities, including the charge recorded for that hit, the position within the strip, the physical width of the strip, the inclination of the track and the magnetic field, among others. This behavior can be understood qualitatively, given a model for the formation of signals on the strips.

Analytical calculations for the formation of signals in cathode strip chambers have been available for many years. Gatti described how charge was apportioned among the strips in 1979 [20]. His calculation was updated and extended by Mathieson and Gordon in 1984 [21].

A simple picture of the signal on three strips labels the charges Q_L, Q_C and Q_R, where by definition the charge on the central strip is larger than that on the left and right side strips. The central strip extends across $-0.5 < s < 0.5$, and the left strip is at $s = -1$ and the right, at $s = +1$. With the muon passing through the central strip slightly to the right of the center of the center strip ($s > 0$), $Q_R > Q_L$, and of course $Q_C > Q_R$.

It is intuitively clear that the position of the muon relates to the relative difference $Q_R - Q_L$, and indeed the first approximation to this position is simply

$$s \approx \frac{1}{2} \frac{Q_R - Q_L}{Q_C - \min(Q_R, Q_L)}. \tag{8}$$

For a justification of this choice, see Ref. [18]. Other choices can be made - this is not critical for the present discussion.

The accuracy of the measurement of s depends on how well the difference $Q_R - Q_L$ can be measured. For the CSC's, most of the charge appears on the central strip, unless the muon passes quite close to the edge of the strip. For the large chambers especially, Q_R and Q_L are only a few percent of Q_C, and in the worse cases are not much larger than the pedestal width. This width characterizes the electronics noise, so the central question is: are the observed charges Q_R and Q_L larger than or comparable to this noise?

If the total charge Q is large, then the impact of the noise will be reduced. This explains why the resolution improves as Q decreases, so long as δ-ray electrons are not interfering with the charge distribution. Explicit calculations show that the resolution should be proportional to $1/Q$ [20, 21].

The charge on the right strip will increase as the muon trajectory approaches $s = 0.5$. In the limit that $s \to 0.5$, Q_L does not matter, and the approximation in Eq. 8 becomes

$$s \approx \frac{1}{2} \frac{Q_R}{Q_C} \to \frac{1}{2}$$

since $Q_R \to Q_C$ in this limit. In such a case, the electronics noise becomes relatively unimportant, since both Q_R and Q_C are substantial. In contradistinction, as the muon trajectory approaches $s = 0$, both Q_L and Q_R are minimal and therefore maximally impacted by electronics noise, making the difference $Q_R - Q_L$ relatively difficult to measure. For these reasons, one expects the best resolution for muon trajectories close to the edge of the strip, and the worst resolution when they go through the center.

The spatial distribution of the charge depends on the separation between strips, for a fixed distance between the strip plane and the anode wire plane. If the physical width of the strip is large, then Q_L and Q_R will be small. Due to the impact of electronics noise, which tends to be larger when the strips are larger, the resolution is poorer in chambers with large strips than in chambers with small strips. For this reason, the strips in the ME$\pm$1/1 chambers have been made particularly small (cf. Table 2), since they play a key role in the momentum measurement in the end caps [1].

Finally, a muon which passes through the anode plane at an oblique angle (with respect to the strips) will produce a relatively broad distribution of charge across the gas gap, leading to a smearing of the distribution of charges Q_L to Q_R, and a poorer resolution.

7.1.3 Qualitative Results from CRAFT

Events were selected which contained a good segment from which residuals distributions for layer 3 could be formed. A good segment was one which contained six rechits and $\chi^2 < 200$ (unreduced). An event was selected if it contained at least one good segment. In order to retain only clean events, any event with more than eight segments of any quality were rejected, as well as events with more than fifty rechits. The event was also rejected if any chamber contained more than four segments of any quality. About 5×10^4 events were selected [6].

Further criteria were applied when filling residuals distributions, to ensure that the results were based on the cleanest possible segments and hits:

1. the estimated errors on the six rechits have to be smaller than 0.2 strip widths. This eliminates rechits based on a single strip or for which the cross-talk correction led to negative values for Q_R and Q_L.

2. The sum of charges for three strips and three time slices for layer 3 could not be too small or too large: $250 < Q_{3\times3} < 1000$ ADC counts.

3. The segment inclination should correspond to tracks originating roughly from the interaction point:
$$-1 < \frac{dy}{dz} < -0.15 \quad \text{and} \quad \left|\frac{dx}{dz}\right| < 0.15 \tag{9}$$
where these are local coordinates: dy/dz is the angle with respect to the anode wires, and dx/dz is the angle with respect to the cathode strips.

4. The strip coordinates were fit to a straight line. The resulting χ^2 value were required to be less than 9 for the 5-hit fit, and less than 50 for the 6-hit fit.

These cuts were relaxed singly when checking the impact of these criteria.

In the remainder of this section, we use the CRAFT data to demonstrate the expected behavior as described in Section 7.1.2. No attempt was made to remove layer-by-layer misalignments, as these are known to be small compared to the resolution.

The "charge" depends on several factors, including the gas composition, pressure, high voltage, amplifier gain, and of course the ionization of the gas by the muon. We denote by $Q_{3\times3}$ the sum of the charges recorded in three time bins across three consecutive strips [18] (left). A distribution of $Q_{3\times3}$ for the CRAFT data is shown in Fig. 16. One ADC count in this figure amounts to approximately XXXXXX pC. The distribution has a long tail, similar to that expected from the Landau distribution.

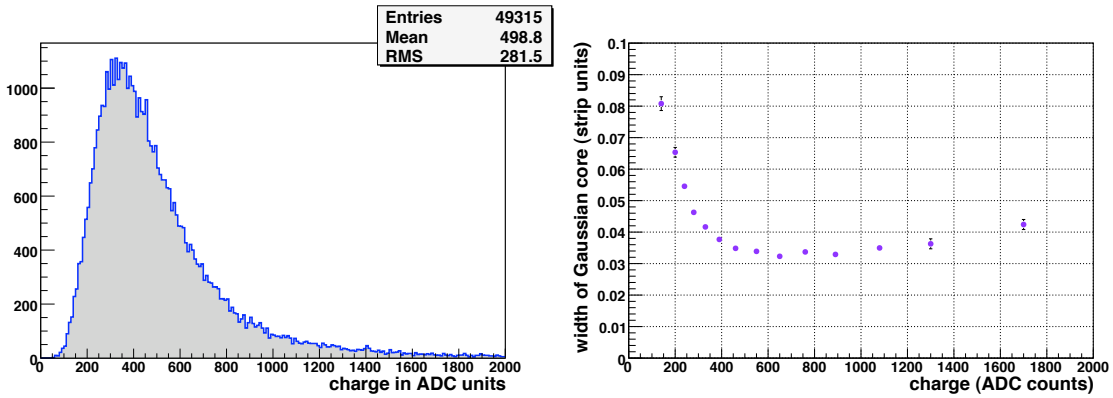

Figure 16: *Left:* observed charge distribution, $Q_{3\times3}$, in ADC counts. *Right:* variation of the *per layer* resolution as a function of $Q_{3\times3}$. This measurement was made using chambers in ME$\pm$2/2 and ME$\pm$3/2; other chambers give very similar results.

A summary of the variation of resolution as a function of charge is given in Fig. 16 (right). Chambers in rings ME$\pm$2/2 and ME$\pm$3/2 were selected for this plot, since they have the largest number of events in CRAFT. The cuts on the χ^2 of the 2-dimensional strip fit were relaxed for this study, so that the impact of δ-ray electrons is clear. If the cuts are imposed, then the rise for $Q_{3\times3} > 800$ ADC counts is eliminated.

Another demonstration of the sensitivity of the resolution to charge is provided by two runs taken outside of the CRAFT exercise, in which the high voltage was raised by 50 V. Since the number of events was modest, the event and segment selection was somewhat looser than described above. The improvement in resolution is consistent with the expected $1/Q$ behavior.

The variation of the resolution with s is shown in Fig. 17. For the ME$\pm$2/2 chambers, the resolution in the center of the strip is worse by about a factor of two than at the edge. This variation is weaker for chambers with thinner strips, such as ME$\pm$1/2 and ME$\pm$1/1.

Most of the analysis presented here is done in terms of the normalized strip width, s. The physical width of the strip matters, too. For broad strips, most of the charge is collected on the central strip, leaving a small amount for Q_L and Q_R, leading to a poorer resolution. For this reason, the smaller chambers have a much better resolution than the larger chambers. Within a chamber, there is a mild variation of the resolution along the strip, since the strip is narrower at the narrow end of the chamber and wider at the broad end.

The results described above were derived for muon trajectories that were nearly perpendicular to the strips. For low-momentum muons coming from the interaction point, however, more oblique trajectories are possible. We have observed a clear variation of the resolution as a function of dx/dz in chambers from ring ME$\pm$2/2, see Fig. 17. For all other results reported in this note, a tight cut on $|dx/dz|$ has been applied.

The estimated uncertainty is computed taking variations as a function of charge, position within a strip, and strip width into account. Distributions of normalized residuals ("pull distributions") allow us to check those calculations. A summary of the pulls for all chamber types is given in Table 3. Overall, the pulls are somewhat too wide, especially for the ME$\pm$1/1 chambers. It will be possible to adjust the error estimates on the basis of the CRAFT data.

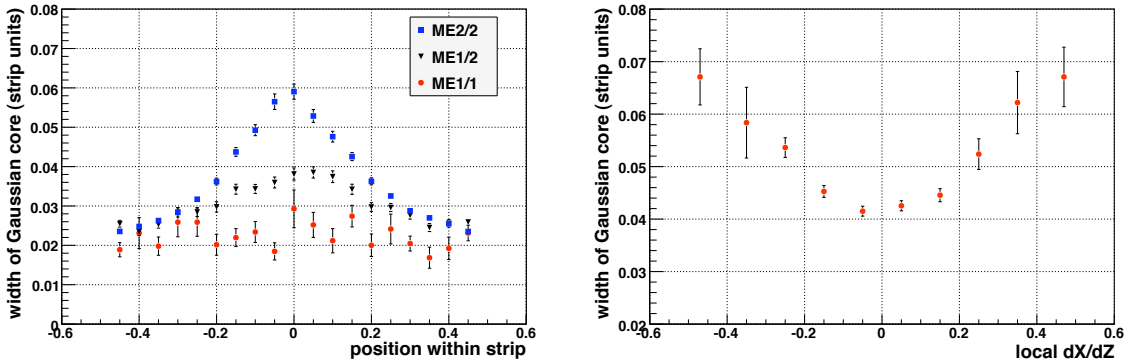

Figure 17: *Left:* variation of the *per layer* resolution as a function of s, the position within the strip, for three different types of chambers. *Right:* variation as a function of local dx/dz, which quantifies the segment inclination with respect to the strips. These measurements were done with the ME$\pm$2/2 chambers.

7.1.4 Measurements of the Nominal Resolution

The results in the previous section demonstrate the expected qualitative behavior of the resolution. In this section, we quantify the resolution of the CSC's, as measured with CRAFT data, in order to verify that they are performing as designed.

Residuals distributions for chambers in each ring were fit to the sum of two Gaussian functions (Eq. 4), and the resolution computed according to Eq. 5. These distributions are shown in Fig. 15. Table 3 lists the *per layer* resolution obtained in this manner. The values given in μm are obtained by multiplying the resolution in strip widths by the average width of the strip (see Table 2).

We formed distributions of χ^2_0 (Eq. 7) for each chamber type. We computed σ_0 (which would be in units of the strip width) and converted to an uncertainty in μm using the average physical strip width. The results are listed in Table 3. These values are somewhat smaller than the values obtained from the fit to two Gaussians.

The resolution of a chamber, given six good rechits, can be estimated on the basis of the *per layer* resolution. One can simply take the numbers listed in Table 3 and divide by $\sqrt{6}$, or one can perform a slightly more refined analysis indicated by Eq. 6. The latter gives systematically lower values for the resolution than the former. Table 4 lists both sets of values, which can be compared to the design values [1]. Most the observed values are somewhat higher, except for the ME$\pm$1/1 chambers, which are significantly better than design. The fact that the high voltage is set to a somewhat reduced value is the primary reason for the slightly worse resolution in the non-ME$\pm$1/1 chambers.

7.1.5 Special Studies of ME1/1

The ME$\pm$1/1 chambers play a special role. First, they prove the key measurements for the high-momentum muon tracks expected at high $|\eta|$. And second, they must operate in a very high magnetic field, which alters the drift of the electrons inside the gas layers. For these reasons, the gas gaps are smaller, the strips are smaller, and the wires are tilted with respect to the chamber bisector [17].

Studies were conducted to check these special characteristics of the ME$\pm$1/1 chambers [7]. The

ring	resolution				pull r.m.s.
	fit to two Gaussians		*derived from* χ^2_0		
	strip widths	μm	strip widths	μm	
ME$\pm$1/1	0.024 ± 0.002	128	0.017	94	1.89 ± 0.06
ME$\pm$1/2	0.034 ± 0.001	285	0.029	245	1.34 ± 0.01
ME$\pm$1/3	0.044 ± 0.001	578	0.041	537	1.52 ± 0.01
ME$\pm$2/1	0.046 ± 0.001	510	0.044	489	1.28 ± 0.02
ME$\pm$2/2	0.040 ± 0.001	487	0.039	474	1.42 ± 0.01
ME$\pm$3/1	0.054 ± 0.002	633	0.052	613	1.26 ± 0.04
ME$\pm$3/2	0.044 ± 0.001	534	0.041	501	1.37 ± 0.02
ME$\pm$4/1	0.054 ± 0.004	648	0.052	625	1.17 ± 0.03

Table 3: resolution *per layer* for each chamber type, and the r.m.s. of the pull distributions

ring	resolution (μm)		
	design	*per layer* / $\sqrt{6}$	Eq. 6
ME$\pm$1/1	75	52	47
ME$\pm$1/2	75	116	110
ME$\pm$1/3	150	234	194
ME$\pm$2/1	150	208	172
ME$\pm$2/2	150	199	169
ME$\pm$3/1	150	258	200
ME$\pm$3/2	150	218	182
ME$\pm$4/1	150	264	221

Table 4: resolution *per chamber* for each chamber type

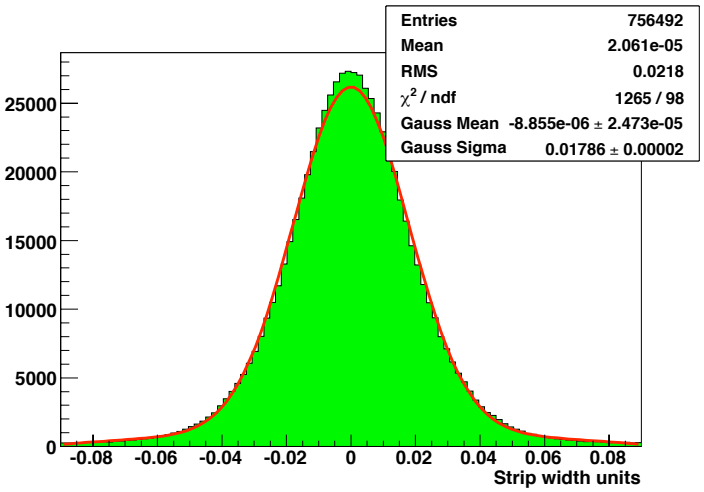

Figure 18: residuals distribution for the ME$\pm$1/1b chambers

selection of suitable events with good segments is very similar to the selection described above. The distribution of residuals in layer 3 is shown in Fig. 18 for ME$\pm$1/1b, with a fit to a single Gaussian and a parabola. Given the mean strip width of 6 mm, this measurement implies a *per layer* resolution of 107 μm, which compares well with the results listed in Table 3. From this value, we estimate a *per chamber* resolution of 50 μm, which is much better than the goal of 75 μm.

The drift of the electrons perpendicular to the anode wires depends sensitively on the magnetic field. Most of the CRAFT data were taken at full field, but some data were taken with zero field, and with some intermediate values. These data were analyzed to measure the resolution as a function of the magnetic field, with the results shown in Fig. 19. Clearly the resolution is best at full field, confirming the initial design.

The radial extent of the ME$\pm$1/1b chambers was divided into four regions in order to check the resolution at different radii. Fig. 19 shows that the resolution is best near the beam line, where it is most critical, and rises rapidly with radius. A further study of the resolution for different azimuthal regions of the ME$\pm$1/1b chambers shows a mild variation with the angle the anode wires, confirming the choices made in the design of these chambers.

7.1.6 Summary

The resolution has been shown to vary with charge, position within the strip, and track inclination in the expected manner. In addition, the variation of the resolution of the ME$\pm$1/1 chambers with magnetic field, radius and wire tilt also has been established. Measurements of the nominal resolution of all eight types of chambers have been completed.

8 Timing

The readout of the cathode strips provides enough information to reconstruct the pulse shape and infer the time of the signal. The output from the cathode strip front-end amplifier is sampled every 50 ns (2 BX) with the results stored in a switched capacitor array (SCA). The arrival of the pulse is arranged so that the first two time bins are free from signal, allowing a dynamical estimate of the signal base line. A good description of the pulse shape recorded in the SCA

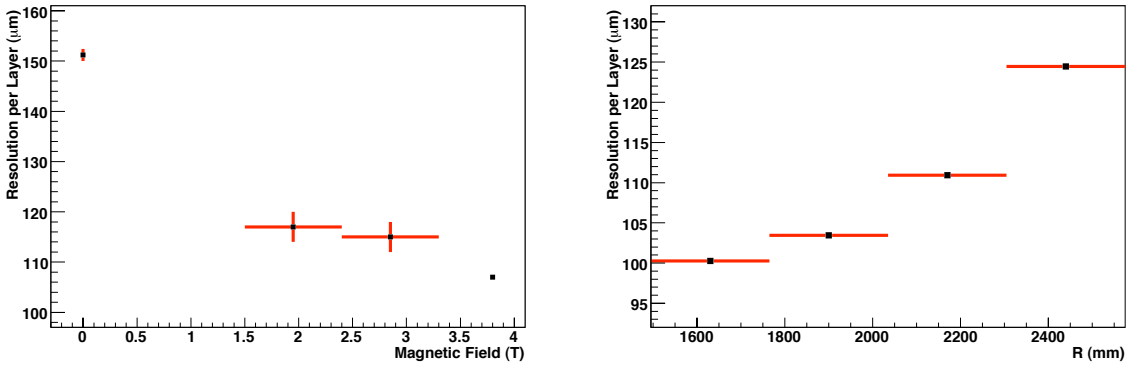

Figure 19: *LEFT:* variation of the resolution in the ME$\pm$1/1b chambers as a function of magnetic field in Tesla. *RIGHT:* variation of the resolution as a function of the radius (distance from the beam line)

is given by a 5-pole semi-Gaussian:

$$S(t) \propto \left(\frac{t - T_S}{T_0}\right)^4 \exp\left(-\frac{(t - T_S)}{T_0}\right)$$

valid for $t > T_S$, the start time. Given the fixed exponent of the $(t - T_S)$ term, the shape of the pulse is determined by the decay constant T_0. The maximum occurs at $t = T_S + 4T_0$.

This pulse shape is very well established through studies with prototypes [19] as well as with cosmic ray data. Cross-talk is approximately 10% of the signal, and should be taken into account in order to describe the pulse shape precisely.

We used the CRAFT data to make some simple tests of the timing capabilities of the CSC's. The time of flight of a muon through a single chamber is quite small, essentially zero compared to the 25 ns BX spacing. Fig. 20 shows the distribution of differences in measured times for layers 6 and 1, in units of 50 ns time bins. The mean is consistent with zero, and the r.m.s. is 0.143 bins, which corresponds to 7.2 ns, or 5 ns per layer. Most segments have six rechits (cf. Fig. 4), so a single segment should have a time resolution of about 2 ns. This compares well with the transit time of a muon from the interaction point to the CSC's of roughly 30 ns.

[These results might be expanded slightly - work is underway.]

Improvements to the use of the strip timing information can be foreseen, based on a more detailed analysis of the subtle effects of cross talk and noise correlations, as suggested by pilot studies with test beam data [19].

It is hoped to use this timing capability for rejecting out-of-time hits and tagging the time of the muon independently of the trigger system.

9 Summary

An assessment of the performance of the CSC's has been completed using the large CRAFT data sample recorded in Fall 2008. Most the the CSC subsystem was in excellent working condition and participated in the bulk of this campaign. The agreement of basic global quantities between the real data and simulation is good. A thorough analysis of the anode signals reveals

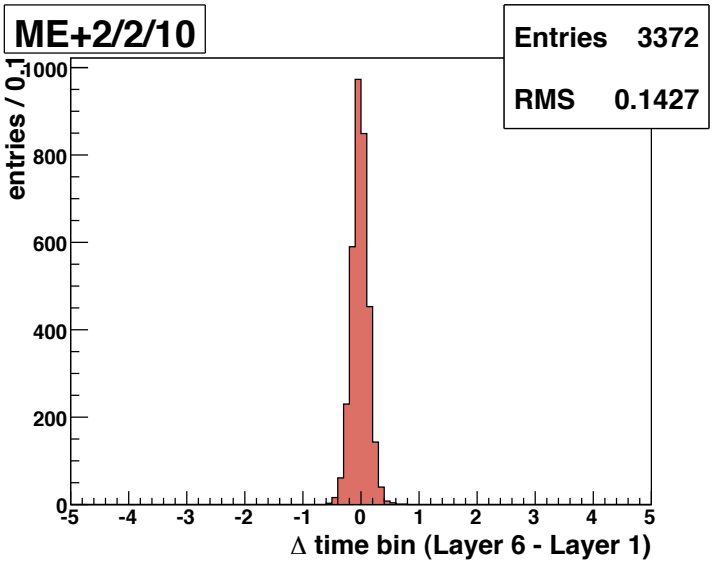

Figure 20: difference in rechit times for layers 6 and 1 in chamber $ME+2/2/10$. Units are 50 ns time bins.

an exceedingly low rate of failure of any kind. All of the essential efficiencies have been measured, ranging from the local charged tracks which trigger the chamber readout through the reconstruction of segments. These efficiencies are all very high. The position resolution has been studied, with variations observed as a function of several relevant variables, such as the charge, position within a strip, high voltage, track inclination, and in the case of the ME$\pm$1/1 chambers, of the magnetic field, radius and wire tilt. The measured chamber resolutions are not quite as good as design, due to an intentional reduction of the high voltage, except for the ME$\pm$1/1 chambers, which surpass the design criterion. Finally, the potential timing capabilities of the CSC's was briefly investigated.

The prospects for future studies are very good. The operating conditions of the CSC subsystem has been improved since the CRAFT data were taken, and one can anticipate that the CSC subsystem will function extremely well once the LHC delivers collisions to CMS.

References

[1] CMS Collaboration, *CMS – The Muon Project*, CERN/LHCC 97-32

[2] CMS Collaboration, *"CMS Physics Technical Design Report"*, CERN/LHCC 2006-001 (2006)

[3] J. Hauser et al., *"Experience with Trigger Electronics for the CSC System of CMS"*, Proceedings of the 10th Workshop on Electronics for LHC Experiments and Future Experiments (2004)

[4] N. Terentiev and T. Ferguson, *Performance of the CMS Endcap Muon Anode-Wire Front-end Electronics in the CRAFT 2008 Data*, CMS-NOTE, submitted

[5] S. Stoynev and M. Schmitt, *Efficiency Measurements in the CSC Muon Endcap System*, CMS-NOTE, in preparation

[6] I. Bloch et al., *Measurement of the CSC Spatial Resolution with Cosmic Ray Muons*, CMS-NOTE, in preparation

[7] V. Perelygin et al., *ME1/1 CSC Spatial Resolution*, CMS NOTE, submitted.

[8] R. Breedon et al., *Post-Production Testing and Commissioning of the CMS End-cap Cathode Strip Chambers*, CMS-NOTE, in preparation

[9] CMS Collaboration, *Studies of CMS Muon Reconstruction Performance with Cosmic Rays*, in preparation

G. Abbiendi et al., *Muon Reconstruction in the CMS Detector*, CMS-AN/2008-097

[10] CMS Collaboration, ALIGNMENT PAPERS

[11] CMS Collaboration, MAGNETIC FIELD MAP PAPER

[12] P. Biallass, T. Hebbeker, K. Hoepfner, *Simulation of Cosmic Muons and Comparison with Data from the Cosmic Challenge using Drift Tube Chambers*, CMS NOTE-2007/024 (2007)

[13] W.-M. Yao et al., Journal of Physics **G33** 1 (2006)

[14] D. Acosta et al., *Large CMS Cathode Strip Chambers: Design and Performance*, Nucl. Instrum. Meth. **A453**, 182-187 (2000).

[15] CMS Collaboration, *The CMS Experiment at the CERN LHC*, Journal of Instrumentation (JINST) **3**, S08004 (2008).

[16] T. Ferguson, N. Terentiev, I. Vorobiev, N. Bondar, A. Golyash, and V. Sedov, *Anode Front-End Electronics for the Cathode Strip Chambers of the CMS Endcap Muon Detector*, Nucl. Instrum. Methods Phys. Res. **A539**, 386-406 (2005) [CMS-Note 2004/003]

[17] Yu V. Erchov et al., *ME1/1 Cathode Strip Chambers*, CMS NOTE 2008/026.

[18] V. Barashko et al., *Fast Algorithm for Track Segment and Hit Reconstruction in the CMS Cathode Strip Chambers*, Nucl. Instr. Meth. **A589/3** (2008) 26 [CMS NOTE 2007/023]

[19] TESTBEAM STUDIES. *Please help specify these.*

[20] E. Gatti et al., *Optimum Geometry for Strip Cathodes or Grids in MWPC for Avalanche Localization Along the Anode Wires*, Nucl. Instrum. Meth. **163** (1979) 83

[21] E. Mathieson and J. Gordon, *Cathode Charge Distributions in Multiwire Chambers: I. Measurement and Theory*, Nucl. Instrum. Meth. **227** (1984) 267; *op. cit.*, *II. Approximate and Empirical Formulae*, Nucl. Instrum. Meth. **227** (1984) 277

[22] D. Acosta et al., *Measuring Muon Reconstruction Efficiency from Data*, CMS NOTE-2006/060 (2006)

R. Breedon et al., *"Efficiency of Finding Muon Track Trigger Primitives in CMS Cathode Strip Chambers"*, Nucl. Instrum. Meth. **A592** (2008) 26 [CMS Note 2007/031]

[These last two papers are not cited???]